Alloys based on Cr-Cr_2Ta containing Si

A. Bhowmik, R.J. Bennett, B. Monserrat,
G.J. Conduit, L.D. Connor, J.E. Parker,
R.P. Thompson, C.N. Jones & H.J. Stone

Alloys based on Cr-Cr$_2$Ta containing Si

Ayan Bhowmik[1][1], Robbie J. Bennett[1], Bartomeu Monserrat[2],

Gareth J. Conduit[2], Leigh D Connor[3], Julia E Parker[3],

Robert P. Thompson[1], C Neil Jones[4], and Howard J. Stone[1]

[1]Department of Materials Science and Metallurgy, University of Cambridge, 27 Charles Babbage Road, Cambridge CB3 0FS, United Kingdom

[2] Department of Physics, Cavendish Laboratory, University of Cambridge, 19 J. J. Thompson Avenue CB3 0HE, United Kingdom

[3] Diamond Light Source, Rutherford Appleton Laboratory

[4] Rolls-Royce plc, P.O. BOX 31, Derby, DE24 8BJ, United Kingdom

Abstract

Cr-Laves phase based dual phase alloys have been considered as potential candidates for high temperature service. This study on these alloys is presented in two sections. In the first part of the paper we investigate the preferential site occupation of Si within the C14 Cr$_2$Ta structure using density functional theory. It has been found that Si substitutes for the Cr atoms rather than Ta within the structure. Si and Cr are relatively free to occupy 2a and 6h sites interchangeably within the structure. However, slight non-uniformity in the 6h Si-Cr minimum charge density and bond length leads to Si favouring 2a occupation within C14 (Cr$_{2-x}$Si$_x$)Ta. High-energy x-ray diffraction also confirmed the same result. Si addition was fond to stabilise the C14 polytype in Cr$_2$Ta. The second part of the paper, reports the microstructures and elevated temperature oxidation characteristics of Cr-Ta-Si-X alloys, where X=Ag, Ti, Hf, Mo, Al and Re. The microstructure of alloys comprised primarily of a eutectic mixture of a Cr-rich solid solution and Cr$_2$Ta-based Laves phase and primary dendrites of C14-Cr$_2$Ta. Upon isothermal exposure of the alloys for 100 h at 1000 ˚C, the Re-containing alloy was found to possess the best oxidation resistance, followed by the Hf-containing alloy. The alloys, however, exhibited a significantly better oxidation resistance at 800 ˚C owing to the formation of an adherent chromia layer The oxidation behaviour of the alloys could be described using a combination of linear and parabolic law.

1 Corresponding author. Tel.: +44 (0) 1223 31950; Fax: +44 (0) 1223 331956
E-mail address: ab754@cam.ac.uk (Ayan Bhowmik)

1   Introduction

Transition-metal Laves phases-based alloys have long been considered for their potential to go beyond Ni-base superalloys in gas turbine engines. If such alloys can be realised that are capable of operating at higher operating temperatures, improved fuel efficiency and cost-effectiveness may be achieved.

Laves phases are intermetallic compounds with the stoichiometry M_2N, an ideal size ratio of N to M of $\sqrt{3/2} \approx 1.225$ (although they might still form between atoms with radius ratio lying between 1.05 and 1.70 [1-4]) and are the largest class of intermetallics. The interest in Laves phases for structural applications at elevated temperatures arises primarily due to their high melting points and thermodynamic stability. However, these phases are typically extremely brittle necessitating the incorporation of a solid solution phase to provide some toughening. In this regard, dual phase alloys based on the eutectics that exist between Cr and Cr_2X (with X=Ta, Nb, Hf etc.) have attracted significant interest owing to their high microstructural stability and good balance of mechanical and oxidation properties [5-7]. Of the various $Cr-Cr_2X$ eutectic based systems, $Cr-Cr_2Ta$ has been identified as offering the benefit of the highest eutectic temperature, fracture toughness and oxidation resistance, which rationalises its advantage over other analogous systems.

In this paper a dual computational and experimental approach has been used to explore quaternary alloys based on Cr-Ta-Si system. Silicon additions have previously been shown to be found to beneficial to mechanical properties of Cr- Cr_2Ta based alloys in terms of hardness and room temperature fracture toughness [8] as well as improving the high temperature oxidation behavior [9]. Silicon additions have also been shown to retard the C14 to C15 polytypic transformation in Cr_2Ta by stabilizing the C14 polytype, thereby preventing any microstructural instability that might arise in the alloys as a result of the polytypic transformation upon long duration of high temperature exposure [10].

In dual phase $Cr-Cr_2Ta$ alloys, silicon partitions preferentially to the hexagonal C14 Laves phase, in which it has extensive solubility. In order to understand the origins of the benefits that may be derived from Si additions, it is informative to understand the sub-lattice sites that Si occupies within the Cr_2Ta crystal. The first step of our study is therefore to perform first principles density functional theory (DFT) to

assess the energy stability of the different substitutional sub-lattice sites available for the Si to occupy.

Whilst ternary Cr-Ta-Si alloys offer improvements over binary Cr-Ta alloys, further improvements may be sought with selected quaternary additions. Hence, in the latter half of this paper, we present the study of quaternary alloys based on Cr-Ta-Si with Ag, Ti, Hf, Mo, Al and Re additions. The microstructural features and isothermal oxidation characteristics of these alloys have been investigated.

Structure of Laves phases

As the crystal structures of Laves phases have significant impact upon the density functional theory (DFT) modelling, review is included on the atomic structure of Laves phases. As the crystal structures of Laves phases have significant impact upon the density functional theory (DFT) modelling, a brief review is included on the atomic structure of Laves phases, particularly of the C14 polytype. A detailed description of the crystal structure, however, has been presented elsewhere [11, 12]. M_2N–type Laves phases are known to crystallise in three different crystal structures, namely C14 (prototype $MgZn_2$), C36 (prototype $MgNi_2$) and C15 (prototype $MgCu_2$). (in Strukturbericht notations). C14 and C36 possess hexagonal unit cells while C15 is cubic. These structures can be best described by stacking atomic layers along the [0001] (for C14 and C36) and the <111> (for C15) directions. The crystal structure of the C14 polytype is given in Figure 1. Within the C14 Cr_2Ta structure, there are the two sub-lattice sites occupied by the smaller Cr, i.e. M, atoms, which are termed as 2a (the so-called 'sandwich layer' according to [11]) and 6h (kagomé layer). The large Ta atom (N), on the other hand, has one sub-lattice site, termed as 4f, which also constitutes the three-layer sandwich unit. The atomic positions within the hexagonal Cr_2Ta are shown in Table 1 as given by Duwez et al [13]. This representation is slightly different from that outlined by Kitano et al. [12]. As can be seen from the table, the origin has been chosen at the 2a layer of Cr-atoms, whereas the kagomé layer has been assigned as the base level, z=0, in [12]. In their representation of the structure, Kitano et al., considered the kagomé layers to occur at z=0 and 1, which is the basic repetitive block and hence accordingly the layers of Ta atoms lie at $z=\pm 3/8$ and the sandwich layer of Cr at z=1/2. But strictly speaking a unit cell of C14 comprises of three kagomé layers i.e. two such repetitive units stacked along the c-axis of the hexagonal structure. As a result of this, within the three-layer sandwich unit, the separation distance between the Cr and Ta atomic layers is $1/12^{th}$ (z=0.062) of c-axis, as seen in Table 1. The layer stacking of the atomic planes could be understood well when viewed down the a-axis i.e. $< 1\bar{2}10 >$ of the hexagon. This projected view is shown in Figure 1 with the different atomic sites labelled.

2   First principle calculations

The first-principles calculations are based on DFT [14, 15]. DFT can reliably and robustly distinguish between different defect configurations for realistically sized systems. We considered three different periodic supercells of a Laves structure with a Si impurity at each of the three defect sites considered (2a, 6h and 4f). Both the supercell shape and the internal atomic positions were allowed to relax. All reported results correspond to calculations of supercells formed by 2x2x1 unit cells, including 48 atoms. Convergence tests were performed with larger supercell sizes, and the energy difference between the different sites is converged to within 10^{-3} eV per atom.

The first-principles calculations were performed within plane-wave DFT [14, 15] using ultrasoft pseudopotentials [16] as implemented in the CASTEP code [17]. The valence electrons of the pseudopotentials are $3s^2\ 3p^6\ 3d^5\ 4s$ for Cr, $5d^3\ 6s^2$ for Ta, and $3s^2\ 3p^2$ for Si. The Perdew-Burke-Ernzerhof (PBE) [18] generalized gradient approximation density functional was used for all calculations. Methfessel-Paxton [19] Fermi surface smearing (cold smearing) of 0.2 eV was applied in order to account for the partial occupancies in metallic systems. Furthermore, an energy cutoff of 450 eV was used, and a reciprocal-space Monkhorst-Pack grid [20] of size 6x6x6. This allowed convergence of all energy differences to within 10^{-5} eV per atom, all forces to 0.05 eV/A and all stresses to 0.1 GPa.

Defect formation energies were calculated using the Wagner-Schottky model [21], which has been adopted elsewhere [22-24]. For a solute species, X^i, occupying the ith (i is either Cr or Ta) site within the lattice, the defect formation enthalpy (hence energy at zero kelvin and pressure) is given as a linear combination of the compound and constituent energies. Thus the energy of formation for a defect within the C14 Cr_2Ta lattice is

$$E_f^d = E_f(Cr_{x_1}Ta_{y_1}X_{1-x_1-y_1}^i)E_f(Cr_{x_0}Ta_{y_0}) + \Delta x E_f(Cr) + \Delta y E_f(Ta) - (1 - x_1 - y_1)E_f(x) \quad (1)$$

Here the values $\Delta x = x_0 - x_1$ and $\Delta y = y_0 - y_1$ are the concentration changes in Cr and Ta respectively between structures with and without solute X, and $E_f(Cr)$, $E_f(Ta)$ and $E_f(X)$ are the energies of formation for the elements in their reference state, shown in Table 2. Using equation (1) it is possible to calculate the defect formation energy for any species X that occupies either Cr or Ta sites within the lattice. The energies of the reference states of Si, Ta and Cr were calculated for the structures listed in table 2. The final lattice parameters (Table 2) are close to previous CASTEP bulk calculations

[25] and within 2% of experimentally determined values [26]. Slight over-binding in Cr and under-binding in Si and Ta was observed. For the structures listed in table 2, the separations of the Si atoms up to 20Å at each of the three wykoff sites, upon cell replication are shown in figure 2. In order to gain the required accuracy for the Wagner-Schottky defect model (i.e. 10^{-3} eV difference per site per atom), the shortest Si-Si bond length has been found to be 8 Å. Clustering of Si atoms then occurs at close to 10 and 13Å. Beyond this Si atoms are not expected to interact significantly.

3 Experimental procedures

3.1 Materials

Solid pieces of high purity elements (99.9 wt.%+) were arc-melted in a water-cooled copper hearth to produce cylindrical ingots of approximately 40g mass. A detailed description of the melting process has been provided elsewhere [8]. The nominal compositions of the alloys investigated are given in Table 3. Ingots were then encapsulated in quartz tubes under an Ar-atmosphere and heat treated at 1100 ˚C for 72h to reduce micro-segregation and to relieve residual solidification stresses induced during processing. The impurity contents of interstitial N and O in the alloys were determined by combustion LECO analysis. The alloys were typically found to contain 0.01-0.04 wt.% O and 1-15 wt. ppm N, which were considered to be within acceptable limits when compared to literature [27]. Alongside these quaternary two phase alloys, a series of some Si-containing monolithic Cr_2Ta ingots were fabricated by arc-melting to study the Si-site occupancy in the Laves phase experimentally. The compositions of selected had the general stoichiometry of $Cr_{66.7-x}Si_x Ta_{33.3}$, where x=10, 15, 20 and 30 at.%, which have been designated as Cr_2Ta-10Si, Cr_2Ta-15Si, Cr_2Ta-20Si and Cr_2Ta-30Si respectively. These samples were then heat treated in fused-silica glass encapsulation under Ar-atmosphere at 1300 ˚C for 200 hrs.

3.2 Methods

3.2.1 Microstuctural characterisation

The annealed ingots were sliced and mounted for microstructural examination or oxidation tests. Microstructural examinations were performed using scanning electron microscopy (SEM) on either a JEOL 5800-LV or a CamScan MX 2600. A Ni calibration standard was used to determine the compositions of the alloys using the

SEM-based energy dispersive spectroscopy (EDS). For selected samples, precise phase compositions were deduced from wavelength dispersive spectroscopy (WDS) using a Cameca SX100 electron probe microanalyser (EPMA). To calibrate the EPMA, pure metal standards were used, and zircon as a Si standard.

3.2.2 High energy x-ray diffraction

The monolithic Laves phases with varying contents of Si were subjected to high energy X-ray beam on the I11 beamline at Diamond Light Source [28, 29]. The I11 detector uses a 15keV operating voltage ($\lambda = 0.826$ Å). The samples were ground into fine powders and stuck on to a 5mm long glass capillary, mounted at the tip of a brass holder, by epoxy resin. The sample is then spun as the diffracted beams are collected by a set of 5 multi-analysing crystal (MAC) detectors each comprising of 9 Si(111) analysing crystals. The experimental set-up is shown in Figure 3. The data is collected at an interval of 0.005° step. Following acquisition, the data was binned into intervals of 3° and Rietveld refinement was performed using TOPAS [30].

3.2.3 Oxidation

The isothermal oxidation kinetics of the alloys was evaluated using thermo-gravimetric analyses (TGA). Samples of the QAV-alloys were cut to dimensions of 4mm × 5mm × 0.2mm and placed inside an alumina crucible. The crucible was suspended by platinum wire within the furnace of a Setaram Setsys DTA equipment that measured the weight change continuously throughout the experiment. Experiments were run on alloys QAV 1-6 at 1000 °C for 100 hours and then the best (QAV-6, Re-addition) and worst (QAV-2, Ti-addition) performing alloys were subjected to an additional tests at 800 °C for 100 h. The ternary Cr-Ta-Si alloy was also subjected to these tests for comparison.

Following high temperature exposure, the cross-sections of the oxidised samples were investigated using SEM and EDS to study the morphology and composition of the oxide layers formed on the surface of the substrates.

4 Results and discussion

4.1 Determination of Si-site occupancy in Cr_2Ta

4.1.1 First principle calculations

The calculated energies of formation for Si site occupation within the C14 Cr_2Ta structure are listed in Table 4. Negative values of -1.86 and -1.72 eV for 2a and 6h Si occupancy respectively indicate energetically favorable sites. A positive value of +0.06 eV for 4f site occupation indicates a marginally un-favourable Ta-Si substitution and so a clear site preference of 2a and 6h for Si substitutions may be expected within the C14 structure. During supercell size optimisation of the laves structure, the energy change upon increasing cell size along the c-axis has been found to be positive, suggesting an attractive Si-Si potential that may lead to Si clustering along this orientation.

To probe the underlying bonding the valence electron density is shown in Figure 4. For both the 2a and 6h Wyckoff sites (Figure 4(a and b)) the Si valence electrons occupy the p-like orbital oriented towards the nearest Cr atoms, whereas for the 4f Wyckoff site (Figure 4c) the valence electrons fill an s-p hybridized orbital reflecting the spherical symmetry of the enveloping Cr atoms. In both structures, the ionic radii for 6-fold coordination of Si^{4+} and Cr^{6+} are 0.40 and 0.44Å respectively. Therefore, by considering only the effective 'size' of cations occupying a given Wyckoff site, Si should freely interchange with Cr. This is in agreement with the EPMA results obtained from Cr-Ta-Si alloys whereby it was observed that increasing Si-content resulted in substitution of Cr within the Laves phase [31]. Bader [32] has demonstrated that the minimum charge density on the line joining the atoms correlates to the strength of bonding so the critical charge density has also been examined. With the Si atom lying on the 4f Wyckoff site the charge density is $0.16Å^{-3}$, whereas for the 2a site the charge density is $0.30Å^{-3}$, exposing the weaker Cr-Si bonds and concomitant higher formation energy of the 4f system. This is corroborated by the Cr-Si separation of 3.1Å in the 4f system that is significantly longer than the 2.64Å bond in the 2a site.

Having discarded the 4f Wyckoff site, attention is now paid to probing the competition between the 2a and 6h sites. In the 2a system the Cr atoms are all equivalent with a minimum charge density of $0.3Å^{-3}$ and bond length of 2.64Å. By comparison, in the 6h system the pair of Cr atoms at 2.57Å are nearer so have a higher

charge density of 0.34Å^{-3}, whereas the Cr atoms at 2.64Å have a charge density of 0.31Å^{-3}, and the furthest pair at 2.66Å have a lower charge density of 0.29Å^{-3}. The asymmetry of the 6h system means that the shortest Si-Cr bonds are stronger and the longest, weaker, compared to the 2a site. Therefore, the energy of the two systems is close, but the overall higher symmetry of the 2a site means that it is more stable.

Further insights into the bonding can be obtained by considering the two co-ordination polyhedra in Figure 4(a-c) between the Si and coordinating Cr/Ta ions. Figure 4(a-c) shows that the Si valence electrons are attracted towards the nearest Cr ions as the p-orbital is stretched towards them. Silicon displays 3sp-orbital hybridization and this phenomena is observed to occur between Si and Cr for Si occupation of 4f Wyckoff sites. For an estimate of bond strength and relative stability between the 2a and 6h Si site occupancies, the minimum charge density has been compared along the line joining the atoms. The results indicate that the lower symmetry of the 6h Si-Cr coordination leads to a small variation in critical charge density and therefore increased instability over 2a Wyckoff Si occupation.

4.1.2 Diffraction results

The diffraction patterns obtained from x-ray diffraction were fitted using TOPAS Rietveld refinement. All the reflections in diffraction spectra collected from the samples could be indexed to the C14 phase. No additional peaks from other polytypes, C36 or C15, were observed in the specimens. However, some additional peaks from a second phase could be observed in the spectrum of the Cr_2Ta-30Si sample, identification of which was not deemed necessary for this study. The existence of only the C14 parameter in the Si-containing Laves phase samples is consistent with some of the early studies reported on dual phase Cr-Cr_2Ta alloys where stabilisation of the C14 polytype is attained by addition of Si [10]. Following a heat treatment of 1300 ˚C for 500 hrs, a binary Cr_2Ta would convert primarily into a cubic C15 polytype with some fraction of residual intermediate higher order polytypes, but addition of Si to Laves phases prevents this structural instability in the phase by resulting in the formation of an extremely stable C14 phase. The results of lattice parameter and Si-anti site occupancies from structural refinement of the C14 phase obtained by fitting the diffraction spectra has been shown in Table 6. An example of Rietveld fitting of the Cr_2Ta-20Si data is shown in Figure 5. As mentioned earlier, most of the samples showed the presence of a single phase C14 with no

9

overlapping reflections from other polytypes, however, with the exception of the Cr_2Ta-20Si sample where a significant majority of the peaks appeared to have an extra edge. A magnified view of a section of the full Cr_2Ta -20Si spectrum is shown in the inset illustrating the effect. These could be accounted by incorporating another variation of C14 polytype in the sample (designated as C14_2). Thus, with increasing Si-content two variations of the C14 polytype could be envisaged to form. These two variants have different lattice parameters and Si-anti site occupations, which imply a local reordering of the phase taking place during prolonged heat treatment through short-range diffusion of the constituent phases. With increasing Si-content there is clearly a decrease in the hexagonal lattice (both a and c) parameters. Si has a high solubility in the Cr_2Ta phase and owing to its small atomic size compared to both Cr and Ta, when it forms an anti-site defect on either Cr or Ta sub-lattice site, it results in an obvious shrinkage in the lattice parameters of the crystal.

Within the Laves phase structure, Si-occupation could occur either on the Cr or the sub-lattice sites. But the Si-ant site defect on the Ta sites had already been shown to be energetically unfavourable by DFT calculations. Thus, while fitting the diffraction data, the Ta occupation was taken to be constant while occupancies on both the Cr sub-lattice sites (2a and 6h) were made to vary. The tabulated results from the structural refinement show a higher Si-occupancy in the 2a Cr site. Also with increasing Si-concentration in the alloy, there is a preference for Si to substitute for Cr in the 2a sites over 6h. Hence, this is in good agreement with the prediction from first principle calculations. Additionally, amongst the two variants of the Laves phase that was observed through the diffraction patterns, C14 and C14_2, there was also a site preference for 2a over 6h for Si – in fact, in the C14_2 variant, Si was primarily found to substitute for the 2a Cr sites only.

This preferential site occupation of Si might have some implications on the structural stability and deformation characteristics of the Laves phase. It is widely accepted that synchronised shear of layers of atoms within the triple layer units of Laves phases by the operation of partials on the basal plane (or (111) planes for cubic C15) is mechanism for polytypic transformation and deformation through twinning and stacking faults [7, 11, 33-35]. The C14 to C15 polytypic transformation in various Laves phase compounds have been shown to occur though such mechanism [36]. The partial occupation of the 2a sites i.e. within the triple layer sandwiched unit of the C14 structure by Si atoms might result restricted synchroshear operation. From the

atomic size viewpoint, a number of studies have hypothesized that the synchroshear movement is facilitated by an increase in the 'atomic-free volume' within the triple layer that reduces the up-down movement of the group of atoms on the adjacent planes [37, 38]. This results in a smoother shearing of the planes and thus an easier structural transformation. The presence of Si, which has a smaller atomic radius compared to Cr, on some of the 2a sites, on contrary, might increase the up-down movement in the sandwich layer, increasing the shear resistance and hence preventing any polytypic transformation. On the other hand, C14-Cr_2Ta Laves phase shows characteristic transformation at high temperatures though synchroshear. It may be further hypothesized that any external shear parallel to the basal plane of the C14 structure would result in the relative movement of the whole sandwich unit, instead of within itself, over the kagomé (single Cr-layer) layer which essentially means stabilisation of the C14 polytype. This proposition, however, warrants detailed microscopic investigation.

4.2 Quaternary alloys based on Cr-Ta-Si

4.2.1 Microstructures of Cr-Ta-Si-X alloys

The microstructure of the quaternary alloys, in general, was observed to be composed of a lamellar eutectic mixture formed between an A2-Cr-rich solid solution and Laves phase and primary dendrites of the Laves phase, see Figure 6. The Laves phase has been observed to exist as the C14 polytype. The alloys have different volume fractions of Laves phase. This is most apparent in QAV-2, to a lesser extent in QAV-5, and QAV-6, and in contrast with QAV-1, QAV-3, and QAV-4, which are close to their eutectic compositions. The higher volume fractions of Cr_2Ta dendrites in QAV-2, 4 and 6 may be attributed, at least in part, with the higher actual Ta contents in these alloys compared to QAV-1, 3 and 5 [39]. Additionally, at higher magnifications, fine sub-micron precipitates of Cr_2Ta were seen within Crrich inter-eutectic regions. These precipitates are likely to have formed as a consequence of Ta enrichment in Cr_2Ta as solidifying eutectic colonies impinge and the subsequent relief of the resultant Ta supersaturation on cooling and during heat treatment. Investigation of individual phase compositions revealed Ti and Al to be partitioned preferentially to the solid solution phase, while the Laves phase is enriched in Hf, Mo, Re.

4.2.2 Oxidation of Cr-Ta-Si-X alloys

Figure 7 shows the TGA curves depicting mass changes per unit area with time for various quaternary alloys following exposure at 1000 ˚C for 100 h. For comparison, the curve for a ternary Cr-10Ta-7Si alloy has also been shown in the plot. The results, in general, show a lower mass change upon oxidation for the quaternary alloys compared to the ternary alloy. Of the quaternary alloys, the Re-containing alloy (QAV-6) showed the best performance, with an overall mass change of ~1.5 mg cm^{-2} followed by the Hf-containing alloy (QAV-3). All of the mass-gain curves are characterised by intermittent steps, indicating brief periods of more rapid mass gain. This had also been previously observed in such Laves phase containing Cr-based alloys [9]. While the overall oxidation curves for the alloys typically show departure from the parabolic oxidation kinetics, the sections of the curves in between the steps can be fitted with a parabolic rate law, consistent with the growth kinetics of the protective chromia layer. While fitting the curves, the linear step jumps were also taken into account besides the intermediate parabolic regions of mass gains. The fitting function used to describe the complete oxidation curves was a combination of linear and parabolic rate laws. The range of parabolic rate constants obtained from fitting various sections of oxidation curves for all the alloys are given in Table 5. As it is evident from the table, the parabolic rate constants for the QAV-6 (Re) alloy at 1000 ˚C is the smallest while that of QAV-2 (Ti) is the greatest. Also, the alloys expectedly show a smaller value of rate constants compared to those at 1000 ˚C owing to a faster oxidation kinetics at higher temperatures. The sections of the curves following a parabolic rate kinetics are believed to correspond to the growth of growth of the chromia layer, which is the major protective oxide for these class of alloys – the linear sections of the curves, on the other hand, pertains to the phase of transient oxidation that involves the growth of the mixed oxide layer. It is to be noted that mixed oxides have been previously observed to form in these dual phase alloys during oxidation at elevated. At the initial stage, isothermal oxidation is generally characterised by a parabolic behaviour attributed to the instant formation of the chromia layer by preferential oxidation of the Cr-solid solution. Following this initial period, as indicated by the mass-gain curves, the overall oxidation of the alloys is the interplay between oxidation of Laves phase constituent by inward diffusion of oxygen through the outer chromia layer into the substrate resulting in the formation of the mixed oxides and continuous formation of chromia layer. The mixed oxides form a

continuous layer underneath the outer chromia layer, particularly after exposure at higher temperatures (> 1100 ˚C) whereas at 1000 ˚C, they are present as discrete particles within the substrate and grow locally upon oxidation of Laves phase particles. The interface between this mixed layer and the substrate alloy is mechanically weak and leads to the detachment of the thermal oxide layer during prolonged thermal exposure. The abrupt increases in the mass change data recorded during isothermal exposure for all of the ternary alloys indicate poor adherence of the thermally grown oxide layer, localised cracking and periodic detachment of the oxide scale from the substrate. No gross spallation of the oxide aggregate was, however, noticed in any of the alloys tested at 1000 ˚C.

Figure 8 shows the cross section of the oxidised QAV-6 alloy, which showed the lowest mass gain of the quaternary alloys investigated. The oxide layer on the substrate is ~10 μm thick, continuous and adherent. In addition, mixed oxides can be seen to have formed on top of the Laves phase particles. This adherent oxide layer might be responsible for an improved oxidation performance of this alloy. Re-addition can possibly be considered effective in better adherence of the oxide layer on top of the substrate, in accordance with the so-called 'reactive element effect'. In contrast, the cross-section of the QAV-2 alloy, the worst performing alloy, shows poor oxide adherence with evidence of extensive subscale cracking. The formation of silica is not observed in any of the oxidised alloys at 1000 ˚C. From the overall mass gain following isothermal exposure at 1000 ˚C for 100 h, even the most oxidation resistant QAV-6 alloy was found to be inferior to the third generation CMSX-4 alloy (~0.2 mg cm^{-2}) [40]. The alloys, however, were found to perform much better at lower temperatures, with the mass gains for the alloys exposed at 800 ˚C for 100 h being about five times lower than that observed at 1000 ˚C, as shown in Figure 9. However, it should be noted that a parabolic law could not adequately describe the oxidation kinetics with the specific mass change as a function of square root of time, not producing a straight line. The mass gains of the alloys at 800 ˚C were found to be comparable to that of CMSX-4 (~0.1 mg cm^{-2}) [40]. As with the tests performed at 1000 ˚C steps were observed in the TGA curves of the alloys at 800 ˚C, although these are smaller than those observed at higher temperature. Figure 10 shows the cross-section of the surfaces of alloys QAV-2 and 6 following oxidation at 800 ˚C for 100 hours. For both alloys, the chromia layer formed on top of the substrates is ~3μm thick with no evidence of subscale cracking.

The oxidation products formed in the quaternary alloys following oxidation at 1000 ˚C has been analysed by x-ray diffraction. The XRD patterns for all the oxidosed samples are shown in Figure 11. The oxide products from alloys were identified to be primarily Cr_2O_3 along with a mixed oxide of Ta_2CrO_6. The mixed oxide is the reaction product of chromia and Ta_2O_5 and forms close to the substrate underneath the outer chromia scale. None of the samples showed formation of silica at 1000 ˚C. In the Al-containing alloy (QAV-5), alumina was not observed to form, suggesting the amount of Al not sufficient to form an oxide scale. XRD analysis were also performed on the samples oxidised at 800 ˚C which showed a spectrum similar to that shown in Figure 11 implying the same oxide products to form in the alloys following exposure at lower temperatures.

5   Summary

The site occupation of Si in the C14 Cr_2Ta structure was studied using first principle DFT calculations and high-energy x-ray diffraction analysis. In addition, the microstructures and oxidation behaviours of some advanced quaternary alloys based on Cr-Ta-Si were reported. The major findings are:

The first principle DFT results are in agreement with experimental observations made in other C14 $MgZn_2$ type compounds, that for the ternary compound $(Cr_{2-x}Si_x)Ta$, Si and Cr are relatively free to occupy 2a and 6h sites interchangeably within the structure. Analysis of the electron localisation surrounding the central Si atom shows 3sp-orbital hybridization with the surrounding Cr ring is not present in either 2a or 6h sites. Slight non-uniformity in the 6h Si-Cr minimum charge density and bond length, leads to Si favouring 2a occupation within C14 $(Cr_{2-x}Si_x)Ta$. The preference of Si for the 2a Cr sites over 6h has also been validated by x-ray diffraction study of a series of monolithic Si-containing Laves phase alloys. Si was found to extensively stabilise the C14 structure with no polytypic transformation products observed even after prolonged exposure at 1300 ˚C. Increasing SI-content in the Laves phase also led to shrinkage of the lattice parameters of the C14 unit cell.

The microstructure of the quaternary alloys based on Cr-Ta-Si containing Ag, Ti, Mo, Hf, Al and Re comprised of a eutectic mixture of a Cr-rich solid solution and Cr_2Ta-based Laves phase and primary dendrites of C14-Cr_2Ta. Upon isothermal exposure for 100 h at 1000 ˚C, the Re-containing alloy was found to possess the best

oxidation resistance, followed by the Hf-containing alloy. Significantly superior oxidation resistance was observed for all the alloys tested at 800 ˚C with an adherent oxide scale. The oxidation behaviour of the alloys could be described using a combination of linear and parabolic law. The oxidation of the alloys at 800 and 1000 ˚C led to the formation of an outer protective chromia scale along with a mixed Ta_2CrO_6 oxide.

Acknowledgements

References

[1] G. Sauthoff, Intermetallics, Wiley-VCH, 1995.
[2] F. Laves, H. Witte, Metall-Wirtschaft, -Wissenschaft und -Technik 14 (1935) 645-653.
[3] A. Sinha, Progress in Materials Science 15 (1972) 81-185.
[4] G. Leitner, G.E.R. Schulze, Kristall und Technik 6 (1971).
[5] M.P. Brady, P.F. Tortorelli, E.A. Payzant, L.R. Walker, Oxidation of Metals 61 (2004) 379-401.
[6] M.P. Brady, J.H. Zhu, C.T. Liu, P.F. Tortorelli, L.R. Walker, Intermetallics 8 (2000) 1111-1118.
[7] K. Kumar, MRS Symposium Proceedings 460 (1997) 667-675.
[8] A. Bhowmik, C.N. Jones, I.M. Edmonds, H.J. Stone, Journal of Alloys and Compounds 530 (2012) 169-177.
[9] A. Bhowmik, H.T. Pang, I.M. Edmonds, C.M.F. Rae, H.J. Stone, Intermetallics 32 (2013) 373-383.
[10] A. Bhowmik, H.J. Stone, Journal of Materials Science 48 (2013) 3283-3293.
[11] K.S. Kumar, P.M. Hazzledine, Intermetallics 12 (2004) 763-770.
[12] Y. Kitano, M. Takata, Y. Komura, Journal of Microscopy 142 (1986) 181-189.
[13] P. Duwez, H. Martens, Trans AIMMPE 194 (1952) 72-74--.
[14] P. Hohenberg, W. Kohn, Phys. Rev. 136 (1964) B864--B871.
[15] W. Kohn, L.J. Sham, Phys. Rev. 140 (1965) A1133--A1138.
[16] D. Vanderbilt, Phys. Rev. B 41 (1990) 7892--7895.
[17] S.J. Clark, M.D. Segall, C.J. Pickard, P.J. Hasnip, M.I.J. Probert, K. Refson, M.C. Payne, Z. Kristallogr. 220 (2005) 567.
[18] P.J. Perdew, K. Burke, M. Ernzerhof, Physical Review Letters 77 (1996) 3865-3868.
[19] M. Methfessel, A.T. Paxton, Physical Review B 40 (1989) 3616-3621.
[20] H.J. Monkhorst, J.D. Pack, Phys. Rev. B 13 (1976) 5188--5192.
[21] S.W.Z. Wagner C, Physik Chem B 11 (1930) 163-210.
[22] K.A. Marino, E.A. Carter, Acta Materialia 56 (2008) 3502-3510.
[23] K.A. Marino, E.A. Carter, Physical Review B 78 (2008) 184105-(184101-184111).
[24] P. Gopal, S.G. Srinivasan, Physical Review B 86 (2012) 014112-.
[25] V. Milman, B. Winkler, J.A. White, C.J. Pickard, M.C. Payne, E.V. Akhmatskaya, R.H. Nobes, International Journal of Quantum Chemistry 77 (2000) 895-910.

[26] D.R. Lide, Ed. CRC Handbook of Chemistry and Physics, CRC Press, 1993.
[27] C.L. Briant, K.S. Kumar, N. Rosenberg, H. Tomioka, International Journal of Refractory Metals and Hard Materials 18 (2000) 9-11.
[28] N. Tartoni, S.P. Thompson, C.C. Tang, B.L. Willis, G.E. Derbyshire, A.G. Wright, S.C. Jaye, J.M. Homer, J.D. Pizzey, A.M.T. Bell, Journal of Synchrotron Radiation 15 (2008) 43-49.
[29] S.P. Thompson, J.E. Parker, J. Potter, T.P. Hill, A. Birt, T.M. Cobb, F. Yuan, C.C. Tang, Review of Scientific Instruments 80 (2009) 0751071-0751079.
[30] http://www.topas-academic.net/.
[31] A. Bhowmik, H.T. Pang, S. Neumeier, H.J. Stone, I. Edmonds, MRS Proceedings 1295 (2011) 323-328.
[32] R.F.W. Bader, Chemical Reviews 91 (1991) 893-928.
[33] P. Hazzledine, P. Pirouz, Scripta Metallurgica et Materialia 28 (1993) 1277-1282.
[34] P. Pirouz, P. Hazzledine, Scripta Metallurgica et Materialia 25 (1991) 1167-1170.
[35] J. Aufrecht, A. Leineweber, V. Duppel, E.J. Mittemeijer, Intermetallics 19 (2011) 1428-1441.
[36] M.F. Chisholm, K.S. Kumar, P.M. Hazzledine, Science 307 (2005) 701-703.
[37] T. Ohta, Y. Kaneno, H. Inoue, T. Takasugi, S. Hanada, Metallurgical and Materials Transactions A 36 (2005) 583-590.
[38] T. Takasugi, M. Yoshida, S. Hanada, Acta Materialia 44 (1996) 669-674.
[39] V. Choda, A. Bhowmik, I.M. Edmonds, C.N. Jones, H.J. Stone, Mater. Res. Soc. Symp. Proc 1516 (2013).
[40] M. Hook, PhD thesis, in: University of Cambridge, 2004.

List of Tables

Table 1: Atomic sites in C14 Cr_2Ta unit cell.

Element	Wycoff notation	Atom positions [13]	Layer
Cr1	2a	0, 0, 0	Sandwich layer
Cr2	6h	0.8305, 0.6610, 0.2500	Kagomé layer
Ta	4f	0.3333, 0.6667, 0.0620	Sandwich layer

Table 2: Structures used for energy calculations using DFT.

Element	Cr	Ta	Si	Cr_2Ta
Space Group	Im-3m	Im-3m	Fm-3m (Diamond)	P63/mmc (194)
Final Lattice parameter (Å)	a=2.848	a=3.363	a=5.468	a=4.925, c=8.106

Table 3: Designation, nominal and actual compositions (in at%) of alloys used in the study.

Alloy designation	Nominal composition (at%)	Measured composition (at%)
QAV-1	Cr-10Ta-7Si-0.5Ag	Cr-6.3Ta-10Si-0.05Ag
QAV-2	Cr-10Ta-7Si-5Ti	Cr-11.5Ta-12.5Si-5Ti
QAV-3	Cr-10Ta-7Si-1Hf	Cr-8.9Ta-11.7Si-0.8Hf
QAV-4	Cr-10Ta-7Si-3Mo	Cr-9Ta-10.5Si-2.8Mo
QAV-5	Cr-10Ta-7Si-3Al	Cr-6.8Ta-9.1Si-2.8Al
QAV-6	Cr-10Ta-7Si-3Re	Cr-9.9Ta-8.4Si-3.4Re

Table 4: Si site defect formation energies.

Wyckoff Position	Defect	E_f (eV)
2a	Si^{Cr}	-1.86
4f	Si^{Ta}	+0.06
6h	Si^{Cr}	-1.72

Table 5: Parabolic rate constants of various alloys subjected to isothermal oxidation tests under two different temperatures 800 and 1000 ˚C). The data for the Cr-10Ta-7Si has been taken from [9].

Alloy	Parabolic rate constants ($g^2cm^{-4}h^{-1}$)	Alloy	Parabolic rate constants ($g^2cm^{-4}h^{-1}$)
Cr-10Ta-7Si, 1000 ˚C	$7.7\times10^{-9} - 4.8\times10^{-8}$	QAV-5, 1000 ˚C	$3.5\times10^{-8} - 3.9\times10^{-8}$
QAV-1, 1000 ˚C	$8.6\times10^{-9} - 3.4\times10^{-8}$	QAV-6, 1000 ˚C	$1.4\times10^{-9} - 9.4\times10^{-9}$
QAV-2, 1000 ˚C	3.9×10^{-8}	QAV-2, 800 ˚C	6.6×10^{-10}
QAV-3, 1000 ˚C	$1.4\times10^{-9} - 1.6\times10^{-8}$	QAV-6, 800 ˚C	3.7×10^{-10}

Table 6: Results of Rietveld refinement of Si-containing Laves phases showing the variation of lattice parameters and Si-occupancies on the Cr sub-lattice sites.

Alloy	Phases					
	C14			C14_2		
	Lattice parameter (Å)	Si-occup. (2a)	Si-occup. (6h)	Lattice parameter (Å)	Si-occup. (2a)	Si-occup. (6h)
Cr_2Ta-10Si	a=b=4.9108 c=8.0340	0.10	0.19	-		
Cr_2Ta-15Si	a=b=4.9090 c=8.0238	0.21	0.13	-		
Cr_2Ta-20Si	a=b=4.8978 c=8.0078	0.56	0.31	a=b=4.8978 c=8.0078	0.43	0.05
Cr_2Ta-30Si	a=b=4.8897 c=7.9854	0.41	0.23	-		
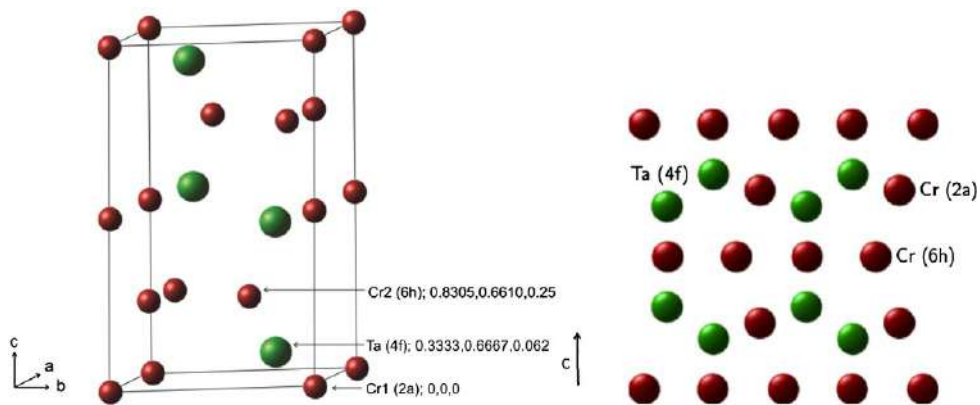
Figure 1. Projected view of C14 structure down the a-axis. The different sub-lattice sites for the Cr (red) and Ta (green) atoms are also labeled.
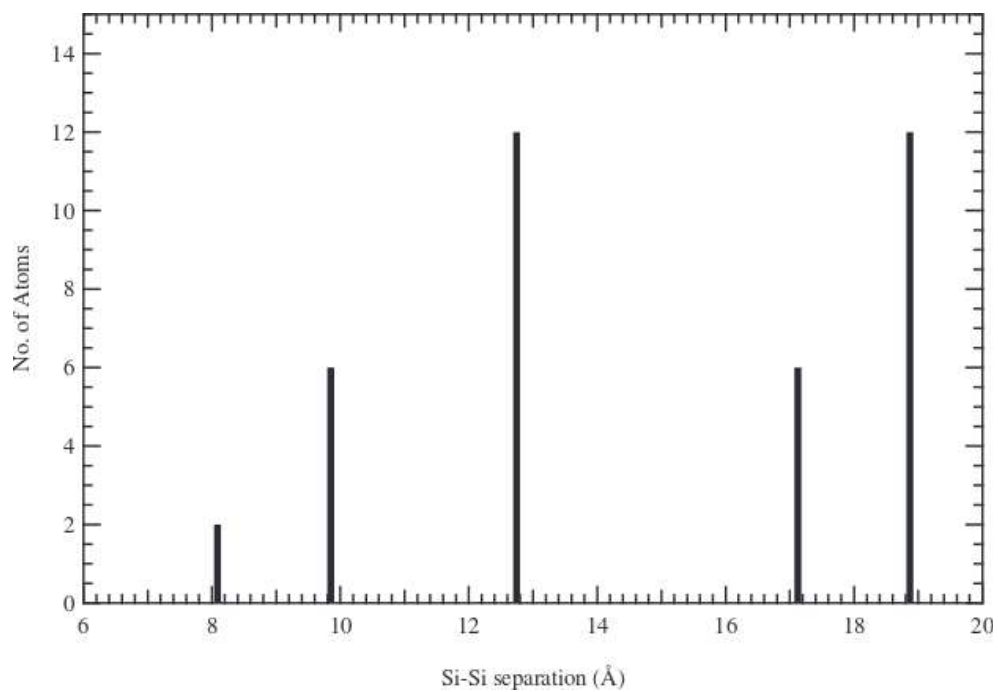
Figure 2. Si-Si separation within the Laves supercell.
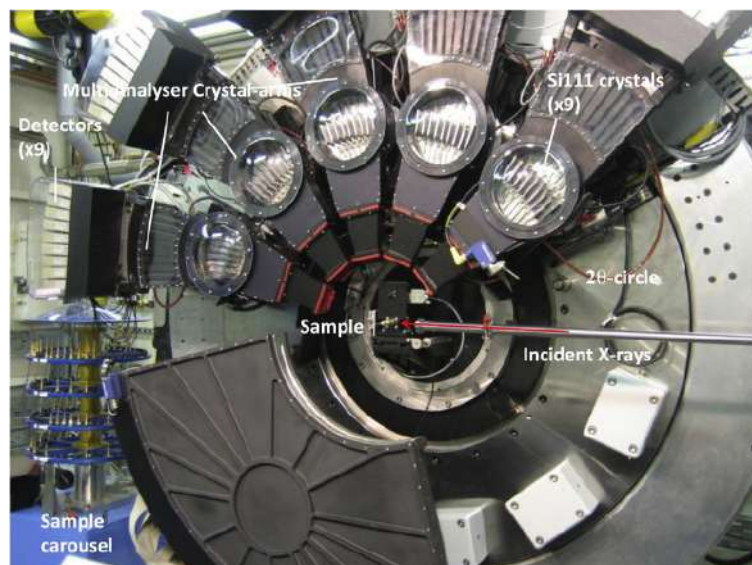
Figure 3. The experimental set-up for beam line I-11 at Diamond with 5 MAC detectors each with 9 Si(111) analysing crystals. The finely powdered sample is stuck onto a glass capillary tube [29].
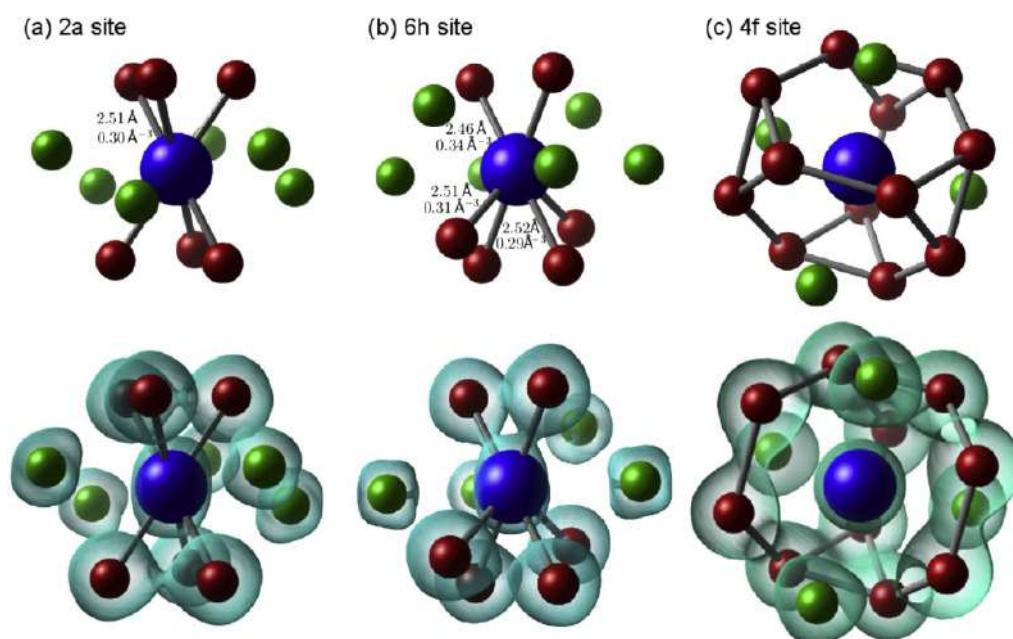
Figure 4. Nearest neighbour Si-Cr bond lengths for 2a (a), 4f (b) and 6h (c) Si occupancies for the fully relaxed Laves structures.
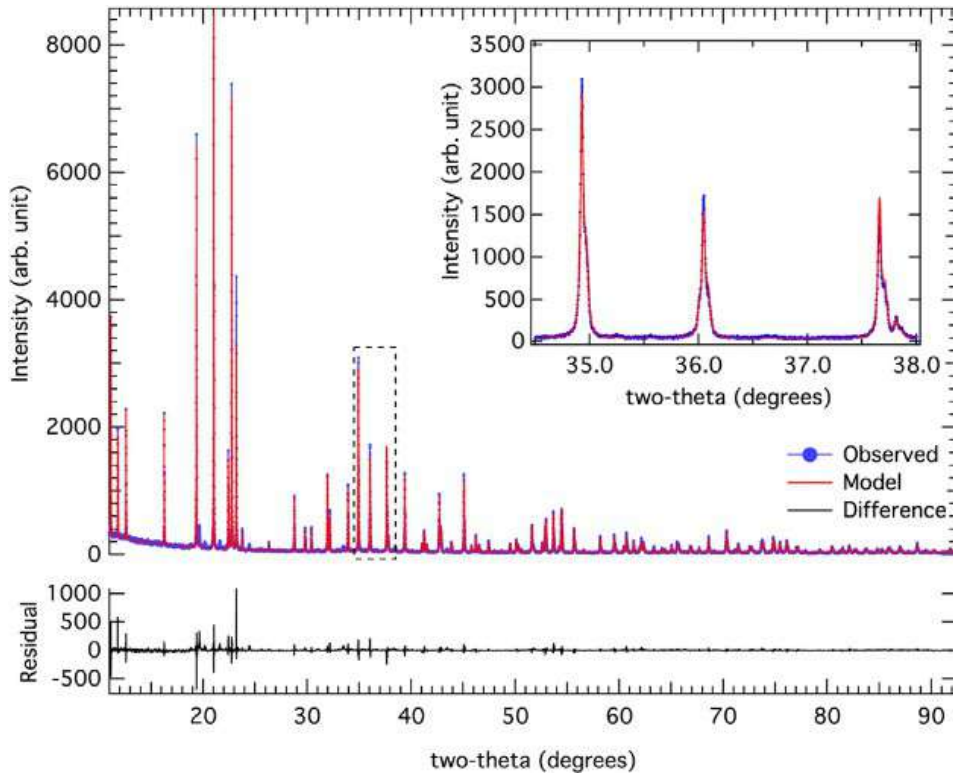
Figure 5. An example of a high energy x-ray diffraction spectrum of Cr_2Ta-20Si sample fitted by Rietveld refinement. A large number of peaks exhibited additional edges, some of which within the dotted rectangle are enlarged in the inset.
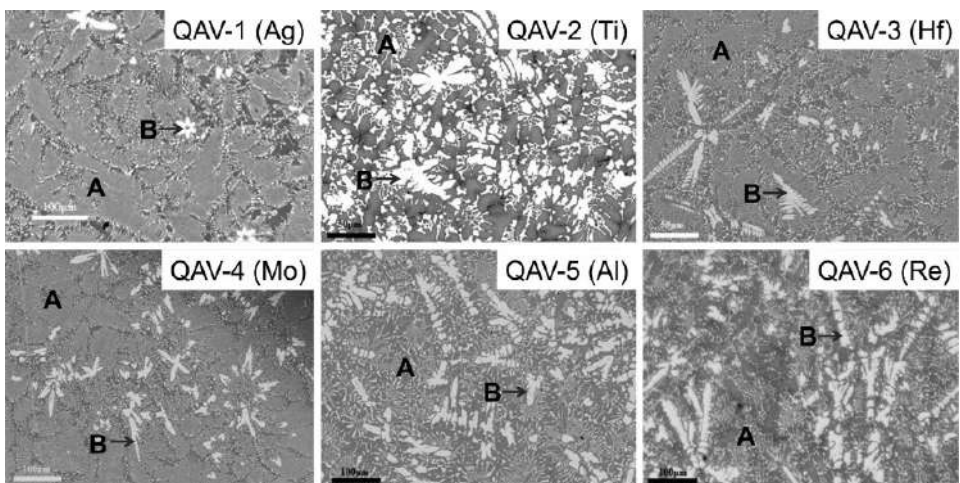
Figure 6. Microstructures of quaternary alloys. 'A' - eutectic mixture and 'B' – Laves phase dendrites.
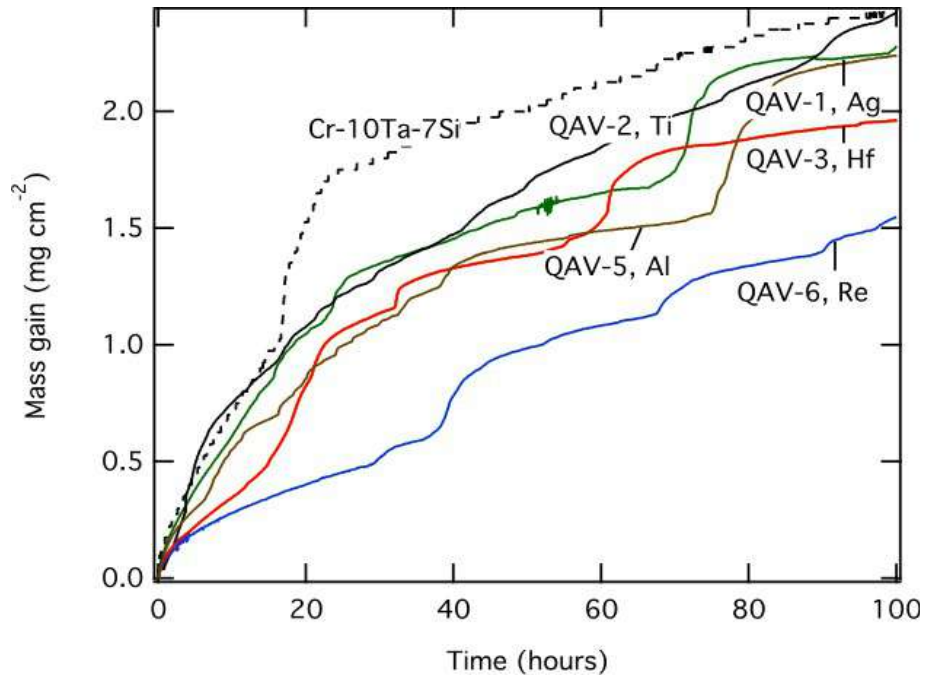
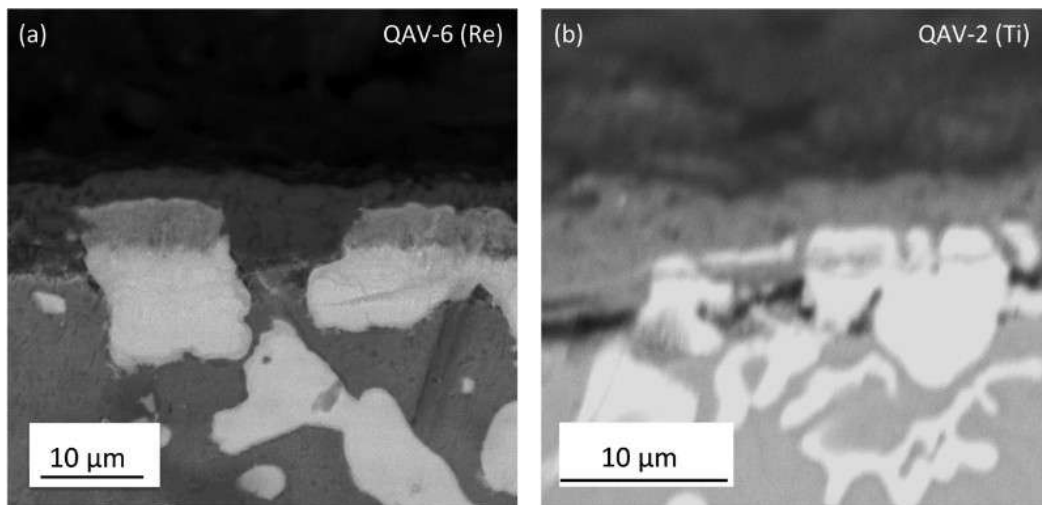Figure 7. Thermogravimetric curves for various quaternary alloys following isothermal exposure at 1000 ˚C for 100 h.

Figure 8. Oxidised cross-sections of (a) QAV-6 and (b) QAV-2 following exposure at 1000 ˚C.
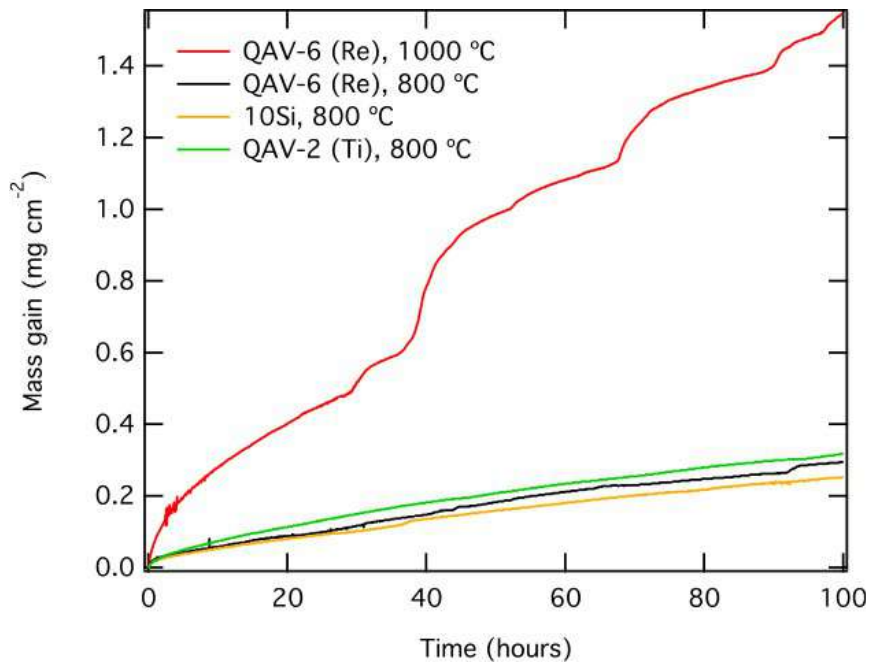
Figure 9. Thermogravimetric curves for QAV-2 and 6 and a ternary Cr-10Ta-10Si (at %) alloys following isothermal exposure at 800 ˚C for 100 h. For comparison, the curve for oxidation of QAV-6 at 1000 ˚C is also shown.
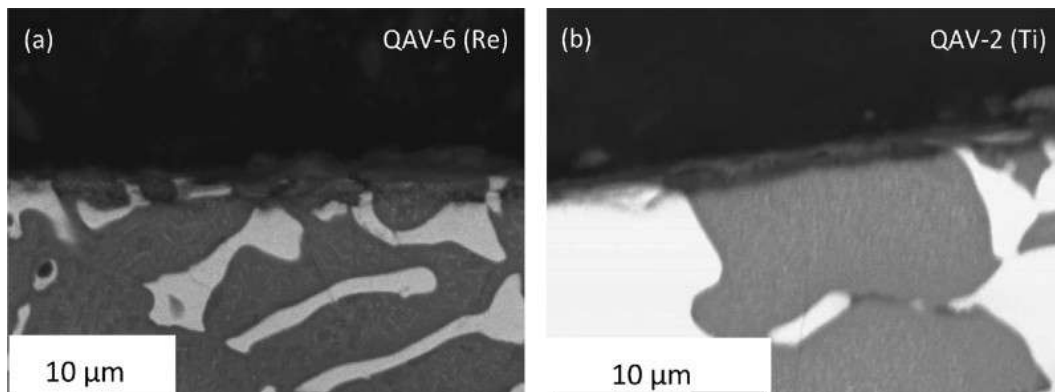

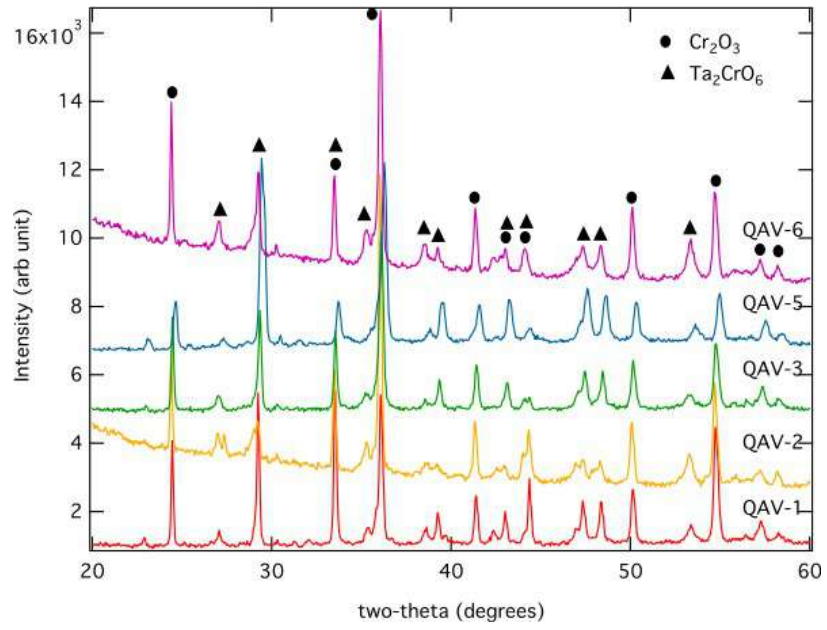Figure 10. Cross-sections of (a) QAV-6 and (b) QAV-2 alloys following oxidation at 800 ˚C.

Figure 11.X-ray diffraction patterns of quaternary alloys oxidised at 1000 ˚C showing peaks from oxidised products.